# The 26 December 2004 tsunami source estimated from satellite radar altimetry and seismic waves

Y. Tony Song,[1] Chen Ji,[2] L.-L. Fu,[1] Victor Zlotnicki,[1] C. K. Shum,[3] Yuchan Yi,[3] and Vala Hjorleifsdottir[2]

Received 2 June 2005; revised 12 September 2005; accepted 16 September 2005; published 18 October 2005.

[1] The 26 December 2004 Indian Ocean tsunami was the first earthquake tsunami of its magnitude to occur since the advent of both digital seismometry and satellite radar altimetry. Both have independently recorded the event from different physical aspects. The seismic data has then been used to estimate the earthquake fault parameters, and a three-dimensional ocean-general-circulation-model (OGCM) coupled with the fault information has been used to simulate the satellite-observed tsunami waves. Here we show that these two datasets consistently provide the tsunami source using independent methodologies of seismic waveform inversion and ocean modeling. Cross-examining the two independent results confirms that the slip function is the most important condition controlling the tsunami strength, while the geometry and the rupture velocity of the tectonic plane determine the spatial patterns of the tsunami. **Citation:** Song, Y. T., C. Ji, L.-L. Fu, V. Zlotnicki, C. K. Shum, Y. Yi, and V. Hjorleifsdottir (2005), The 26 December 2004 tsunami source estimated from satellite radar altimetry and seismic waves, *Geophys. Res. Lett.*, *32*, L20601, doi:10.1029/2005GL023683.

## 1. Introduction

[2] Earthquake tsunamis are difficult to predict because the mechanism of undersea earthquakes is poorly understood and the resulting force that triggers a tsunami is difficult to measure [*Mofjeld et al.*, 1999]. Even several months after the devastating tsunami of the 26 December 2004 Sumatra-Andaman earthquake, the precise tsunami source and generation mechanism are still unknown [*Lay et al.*, 2005; *Ammon et al.*, 2005]. Nevertheless, numerical models play a fundamental role in tsunami research [*Shuto*, 1991; *Johnson*, 1999]. Most tsunami models are based on two-dimensional shallow water equations [*Satake*, 1995]. To simulate earthquake tsunamis, models are often initialized by an instantaneous perturbation on the sea surface. The surface perturbation is assumed to exactly match the vertical component of the seafloor deformation due to faulting [*Abe*, 1973; *Satake*, 1994]. Specifically, the deformation is estimated from the seismic moment, $M_o = \mu AD$, where $\mu$ is the fault rigidity, $A$ is the fault area, and $D$ is the average displacement across the fault. The initially estimated seismic moment for the December earthquake is $4.0 \times 10^{22}$ Nm ($M_w = 9.0$) and gives the displacement 5 meters, while the upgraded moment $8.2 \times 10^{22}$ Nm ($M_w = 9.2$) gives the displacement 10 meters, both using the estimated fault area $200 \times 1300$ km$^2$ and rigidity $3.0 \times 10^{10}$ N/m$^2$ [*Lay et al.*, 2005]. Obviously, there is a great uncertainty in quantifying the vertical component from the total displacement. Although this approach has been widely used in tsunami studies [*Johnson*, 1999], attempts to match observations have been disappointing [*Mofjeld et al.*, 1999]. For instance, the modeled tsunami based on the seismic estimation of the 1992 Nicaraguan earthquake is several times smaller than the actual measurement of tide gauges [*Imamura et al.*, 1993].

[3] This study differs from previous studies in three aspects: First, the seismic waveform inversion [*Ji et al.*, 2002] is used to obtain the three-dimensional seafloor displacements of the earthquake [*Ammon et al.*, 2005]. Second, a three-dimensional ocean-general-circulation-model (OGCM) is employed to couple the waveform inversion and therefore captures the full earthquake forcing at the ocean bottom [*Voit*, 1987; *Kanamori and Kikuchi*, 1993; *Tanioka and Satake*, 1996]. Third, satellite observations in the open ocean will be used to verify the seismic inversion and model simulation. By cross-examining the two independent results and comparing with the satellite observations, we are able to obtain the best possible information on the rupture history of the earthquake, which provides insight into the earthquake-tsunami generation mechanism and allow us to demonstrate the possibility of using the modern seismic data and state-of-the-art modeling technologies for future tsunami prediction.

## 2. Method and Data

### 2.1. Seismic Waveform Inversion

[4] The seismic waves generated by the December earthquake were recorded by more than a hundred high-dynamic-range broadband seismic stations worldwide, under the Global Seismographic Network [*Park et al.*, 2005]. The waves received by a given station, depending on its location and distance to the earthquake source, carry information on the nature of the fault plane motion and can be used to invert the earthquake source. Based on the finite-fault inversion theory [*Olson and Apsel*, 1982; *Hartzell and Heaton*, 1983], the seismic and static response of a finite-size fault plane can be

[1]Jet Propulsion Laboratory, California Institute of Technology, Pasadena, California, USA.
[2]Seismological Laboratory, California Institute of Technology, Pasadena, California, USA.
[3]Space Geodesy and Remote Sensing, Ohio State University, Columbus, Ohio, USA.

Copyright 2005 by the American Geophysical Union.
0094-8276/05/2005GL023683

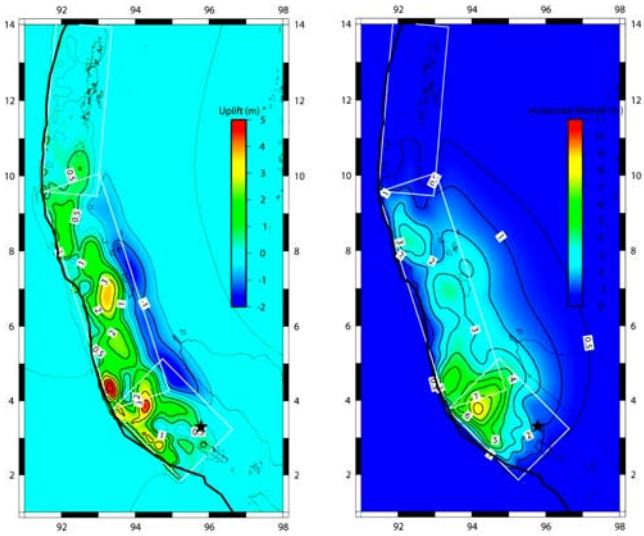


**Figure 1.** Seismically-inverted seafloor motions: left panel shows the vertical displacement with a maximum of 5 meters and right panel shows the horizontal displacement with a maximum of 11 meters. Color bars represent the contour intervals in meters. The star is the deep epicenter and the heavy black curve is the fault line. White boxes represent the Sumatra, Nicobar and Andaman segment, respectively.

represented by a summation of contributions from the subfaults,

$$u(t) = \sum_{j=1}^{n} \sum_{k=1}^{n} D_{jk} \left\{ \cos(\lambda_{jk}) Y_{jk}^{1}(V_{jk}, t) + \sin(\lambda_{jk}) Y_{jk}^{2}(V_{jk}, t) \right\} S_{jk}(t) \tag{1}$$

where $D_{jk}$ is the slip amplitude, $\lambda_{jk}$ is the rake angle, $S_{jk}$ is the rise time function, $V_{jk}$ is the average rupture velocity between the hypocenter and the subfault jk, and $Y^{i}_{jk}(V_{jk}, t)$ are subfault Green's functions for the unit slip in the strike direction and down-dip direction. The waveform inversion has been performed in the wavelet domain instead of in the traditional time or frequency domain, and takes full advantage of the broadband characteristics of modern seismic records by simultaneously extracting useful information while depressing noise [*Ji et al.*, 2002, 2004]. Figure 1 gives the seismically-inverted three-dimensional seafloor motions of the December earthquake. The waveform inversion reveals a strongly heterogeneous slip distribution. Most of the slip is concentrated on the slope off Sumatra. However, this earthquake is undersea; thus the inversion is difficult to be verified by conventional methods used over land, e.g., synthetic aperture radar interferometry (InSAR). In addition, the inversion is static and the exact rupture history is largely unknown.

### 2.2. Ocean Modeling

[5] Our three-dimensional OGCM, widely used in studying oceanic dynamics [*Song and Haidvogel*, 1994], has an important bottom-pressure-following feature [*Song and Hou*, 2006] for tsunami simulations because accurate topography is needed to apply the earthquake forcing. In addition, the December Sumatra-Andaman earthquake (the main shock and aftershocks) has unusually long rupture durations [*Ammon et al.*, 2005], while the seismically-inverted solution is static and does not have the complete information of the rupture process for initialing the ocean model (Note: Dynamic solution has been computed later and been used in a separate study.) For these reasons, we propose a dynamic seafloor motion by decomposing the fault area into $n$ subfaults:

$$\delta h(x, y, t) = \sum_{i=1}^{n} g_z(x, y) \gamma_i(t) \tag{2}$$

where $x$ and $y$ represent the longitude and latitude, respectively, $\gamma_i(t)$ is the slip function of the $i$th subfault and represents the rupture strength at a given time $t$ in a step-function form, and $g_z(x, y)$ is the normalized upward component of the subfault movement and an analytical fit of the vertical displacement (the left panel of Figure 1). Similarly, the horizontal seafloor motions are obtained through the eastward and northward components, $g_x(x, y)$ and $g_y(x, y)$, computed from the horizontal displacements (the right panel of Figure 1). The total fault slip is then represented by the summation of all rising/dipping subfaults along the fault line, and only the slip function remains to be determined (which will be discussed later). In this way, the seismically-inverted solution is decomposed into three-dimensional seafloor motions, which are applied to the ocean model as a sequence of instantaneous body force, as represented by the eastward body-force $F_u$, northward body-force $F_v$, and bottom-pressure $P_b$ in the basic ocean equations of *Song and Hou* [2006]. Based on the hydrostatic relation, the sea-surface-height (SSH) anomaly is diagnosed from the bottom-pressure changes and will be compared with the satellite observations.

### 2.3. Satellite Data

[6] On 26 December 2004, several satellites carrying radar altimeters passed over the Indian Ocean [*Gower*, 2005]. As the tsunami waves were rolling toward the shore, these satellites recorded the SSH change of the waves as they propagated. Different from conventional observations, such as the tide gauges [*Johnson*, 1999], the satellite observations in the open ocean were closer to the earthquake source and represented continuous profiles of SSH change. These unique observations in the open oceans are critical for estimating the tsunami source and for testing tsunami prediction models. However, the satellite observations contain non-tsunami-related signals of ocean dynamics caused by wind and eddies [*Fu and Cazenave*, 2001; *Shum et al.*, 1995]. To isolate the tsunami-only signals, we first run the OGCM without the earthquake forcing for the ocean dynamics and then remove the non-tsunami signals from the satellite data and the model runs with the earthquake forcing. Although several satellites have observed the tsunami, only two tracks are used: Jason-1 track 129 and ENVISAT track 352. These two tracks are the most complete and closest to the fault area, thus giving us the most reliable information on the tsunami source.

## 3. Sensitivity Study

[7] To determine the dynamic seafloor motions, we have carried out a series of sensitivity studies based on a



19448007, 2005, 20, Downloaded from https://agupubs.onlinelibrary.wiley.com/doi/10.1029/2005GL023683 by RH-net, Wiley Online Library on [09/11/2026]. See the Terms and Conditions (https://onlinelibrary.wiley.com/terms-and-conditions) on Wiley Online Library for rules of use; OA articles are governed by the applicable Creative Commons License

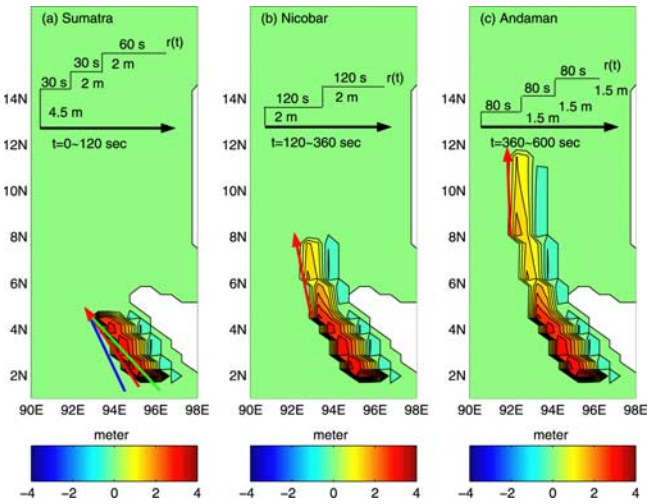



**Figure 2.** Schematics of slip function $r(t)$ and rupture scenario estimated from satellite observations: (a) Sumatra segment ruptured from 0 to 120 seconds; (b) Nicobar segment ruptured from 120 to 360 seconds; (c) Andaman segment ruptured from 360 to 600 seconds. Red arrows indicate the strike direction along the fault line. The blue and green lines in the Sumatra segment are the right and left-shifted fault orientation. Color bars are the scales of the vertical component of the seafloor motions.

simplified structure of fault plane in terms of a group of subfaults (n = 8), as shown in Figure 2. Specifically, we group the subfaults into three segments: the Sumatra segment (2°N∼5°N) in the south, the Nicobar segment (5°N∼8°N) in the middle and the Andaman segment (8°N∼12°N) in the north. The rupture of a segment is represented by a sequence of subfault motions. The rupture front is simulated to propagate north-westward and then northward from the epicenter near the Sumatra to the Andaman Islands, with an averaged rupture velocity of 3.5 km/s, 1.25 km/s and 1.5 km/s in the three segments, respectively. The sensitivity study has focused on the four faulting parameters: fault orientation, length, rupture duration, and slip function. The values best matching the satellite observations will be determined.

[8] Figure 3a: Fault orientation (Fault-O) determines the travel direction of the fault strike. Here, we test the fault line in three positions by shifting the Sumatra segment 80 km to the left (green line position) or to the right (blue line position). The results show that the fault orientation not only affects the amplitude, but also the patterns of the tsunami. The left/right-shifted fault decreases/increases the southern edge of the tsunami along the Jason-1 pass, indicating a directional shift of the tsunami intensity. This might explain why there was much less damage to the coasts of Bangladesh and Australia than to the coasts of Thailand and Sri Lanka. This directionality of tsunami intensity also adds uncertainties to the tsunami warning system, particularly if the system is based on sparse in-situ measurements, because measurements at wrong locations may significantly underestimate the strength of the tsunami. Therefore, seismic source and model simulation should be combined to estimate the full strength and spatial patterns of a tsunami for reliable warnings.

[9] Figure 3b: Fault length (Fault-L) is one of the important earthquake parameters that determines the seismic moment of the quake. Here, we test three cases by assuming the effective rupture ends at 5°N (∼400 km), 9°N (∼800 km), and 15°N (∼1400 km), respectively. Surprisingly, the strength of the tsunami changes relatively little, only 10% in the peak of the leading wave. However, they have different features in the northern part of the tsunami. The 400 km fault length does not generate the two northern waves observed by the Jason satellite, indicating the rupture that has been researched further north. On the other hand, the 1400 km fault case shows an inconsistently stronger tsunami compared to observation, indicating that either a rupture further north did not occur, or, if it occurred, it did not generate a significant tsunami.

[10] Figure 3c: Rupture duration (Fault-T) is also tested. It is shown that the tsunami strength is not particularly sensitive to the total rupture time. The threshold time, beyond which the same fault rupture would not generate a significant tsunami, is about 50 minutes. However, the wave patterns are very sensitive to the rupture velocity. The reason is that the rupture speed (∼2 km/s) is about 10 times of the wave propagation speed (∼200 m/s). Based on the two speeds, it can be estimated that the leading tsunami wave in the southern part of the Jason-1 track was caused by the quake in Sumatra and the northern small waves were caused by the aftershocks in Nicobar and Andaman.

[11] Figure 3d: Slip function (Fault-H) is found to be the parameter to which the tsunami strength is most sensitive because it determines the slip distance and speed. A slight change of its maximum value, from 4 m to 5 m or to 3 m, can significantly alter the strength of the tsunami. We have also shown that for the given geometry of the tectonic plane, the threshold for generating the tsunami waves is

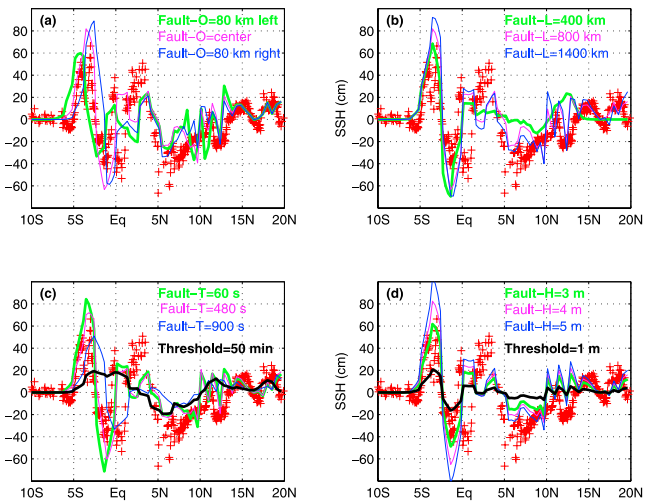



**Figure 3.** Tsunami sensitivity to fault parameters: (a) fault orientation, (b) fault length, (c) rupture duration, and (d) slip function. Each panel gives the sensitivity to the present parameter with other three parameters fixed at the middle value. The black curves are the threshold for generating significant tsunami signals with respect to the typical magnitude of sea-surface variation (∼20 cm).



19448007, 2005, 20, Downloaded from https://agupubs.onlinelibrary.wiley.com/doi/10.1029/2005GL023683 by RH-net, Wiley Online Library on [09/11/2026]. See the Terms and Conditions (https://onlinelibrary.wiley.com/terms-and-conditions) on Wiley Online Library for rules of use; OA articles are governed by the applicable Creative Commons License

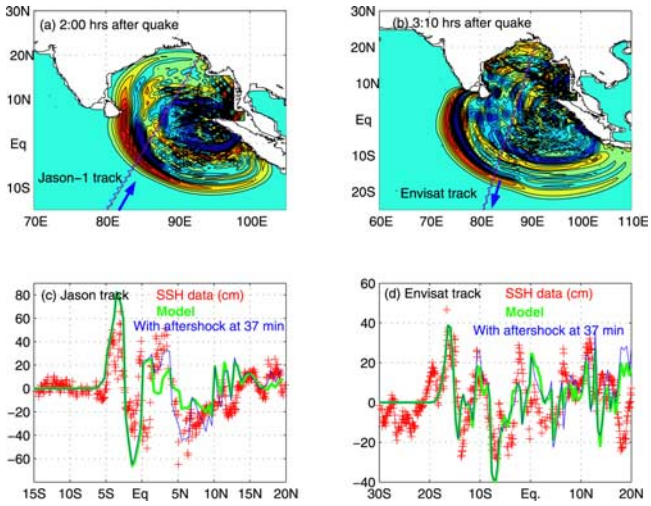



**Figure 4.** Comparison between model and satellite observations: (a) model tsunami and Jason-1 track at 2:00 hours after the initial quake, (b) model tsunami and ENIVSAT track at 3:10 hours after the initial quake, (c) sea-surface profiles along Jason-1 track, and (d) sea-surface profiles along ENVISAT tack. Red crosses are satellite data and green lines are the model results. Blue lines are the model results with an aftershock at 93°E and 6°N about 37 minutes after the first quake. Units are in centimeters.

about 1 m. This indicates that the estimate of the slip function from seismic data is the most important parameter for tsunami prediction.

## 4. Discussion and Summary

[12] From the sensitivity experiments, we obtain a set of optimal parameters for coupling the seismically-inverted solution with the ocean model. Figure 4 displays the model results based on the seismic inversion and the optimal parameters. Comparison with the satellite observations shows that the model captures the leading wave of the tsunami well, but fails to match the second wave height (at 3°N) along the Jason-1 track and the waves in the northern end (at 18°N) along the ENVISAT track. The mismatches in the northern end are probably due to the poor resolution of the model coastline. In addition, there is a time mismatch of about a few minutes toward the northern end due to the travel time of satellites. However, the seismically-inverted solution does not properly capture the strength of the second crest and trough of the tsunami, particularly along the Jason-1 track. Seismograms have indicated that the total rupture process has lasted at least 1000 seconds, and as long as 3600 seconds [*Park et al.*, 2005]. Such a long process of earthquakes has provided both technical and computational challenges to the inversion model. The period from the leading tsunami wave to the second one is about 37 minutes [*Gower*, 2005]. By adding an aftershock at 93°E and 6°N about 37 minutes after the first quake, the simulation, shown by the blue lines, is clearly better than that without the aftershock. Such an event may also be possibly triggered by a series of landslides [*Jiang and LeBlond*, 1994].

[13] In summary, this study has demonstrated, for the first time, that a three-dimensional OGCM can be coupled with the seismic waveform inversion to study tsunamis. The coupled earthquake-OGCM has two advantages over the conventional tsunami wave models: (1) three-dimensional seismically-inverted solutions can be fully incorporated and (2) ocean dynamics contained in the satellite observations can be removed to isolate the tsunami-only signals. Furthermore, this study also has successfully demonstrated that satellite observations can be used to gain insight into the undersea earthquake source. However, a disadvantage of using three-dimensional OGCMs is the expensive computational cost, though the expense can be dramatically reduced in the future with fast growing computing technology. In fact, OGCMs are usually operated in near real-time at many institutions around the world, have increased resolution in regions of interest to those institutions, and can be better used to provide early warnings for their coastal regions at risk.

[14] **Acknowledgments.** The research described here was conducted at the Jet Propulsion Laboratory, California Institute of Technology, under contract with the National Aeronautics and Space Administration (NASA). Constructive comments from Jeroen Tromp and Ichiro Fukumori are appreciated.

## References

Abe, K. (1973), Tsunami and mechanism of great earthquakes, *Phys. Earth Planet. Inter.*, *7*, 143–153.

Ammon, C. J., et al. (2005), Rupture process of the 2004 Sumatra-Andaman earthquake, *Science*, *308*, 1133–1139.

Fu, L.-L., and A. Cazenave (Eds.) (2001), *Satellite Altimetry and Earth Sciences: A Handbook of Techniques and Applications*, 463 pp., Elsevier, New York.

Gower, J. (2005), Jason 1 detects the 26 December 2004 tsunami, *Eos Trans. AGU*, *86*(4), 37.

Hartzell, S. H., and T. H. Heaton (1983), Inversion of strong ground motion and teleseismic waveform data for the fault rupture history of the 1979 Imperial Valley, California earthquake, *Bull. Seismol. Soc. Am.*, *73*, 1553–1583.

Imamura, F., N. Shuto, S. Ide, Y. Yoshida, and K. Abe (1993), Estimate of the tsunami source of the 1992 Nicaraguan earthquake from tsunami data, *Geophys. Res. Lett.*, *20*, 1515–1518.

Ji, C., D. J. Wald, and D. V. Helmberger (2002), Source description of the 1999 Hector Mine, California, earthquake, part I: Wavelet domain inversion theory and resolution analysis, *Bull. Seismol. Soc. Am.*, *92*, 1192–1207.

Ji, C., D. V. Helmberger, and D. J. Wald (2004), A teleseismic study of the 2002 Denali fault, Alaska, earthquake and implications for rapid strong-motion estimation, *Earthquake Spectra*, *20*(3), 617–637.

Jiang, L., and P. H. LeBlond (1994), Three-dimensional modeling of tsunami generation due to a submarine mudslide, *J. Phys. Oceanogr.*, *24*, 559–572.

Johnson, J. M. (1999), Heterogeneous coupling along Alaska-Aleutians as inferred from tsunami, seismic, and geodetic inversions, *Adv. Geophys.*, *39*, 1–116.

Kanamori, H., and M. Kikuchi (1993), The 1992 Nicaragua earthquake: A slow earthquake associated with subducted sediments, *Nature*, *361*, 714–716.

Lay, T., et al. (2005), The great Sumatra-Andaman earthquake of 26 December 2004, *Science*, *308*, 1127–1133.

Mofjeld, H. O., F. I. Gonzalez, and J. C. Newman (1999), Tsunami prediction in U.S. coastal regions, in *Coastal Ocean Prediction*, *Coastal Estuarine Ser.*, vol. 56, edited by C. N. K. Mooers, pp. 353–375, AGU, Washington, D. C.

Olson, A. H., and R. Apsel (1982), Finite fault and inversion theory with applications to the 1 979 Imperial Valley earthquake, *Bull. Seismol. Soc. Am.*, *72*, 1969–2001.

Park, J., K. Anderson, R. Aster, R. Butler, T. Lay, and D. Simpson (2005), Global Seismographic Network records the Great Sumatra-Andaman earthquake, *Eos Trans. AGU*, *86*(6), 60.

Satake, K. (1994), Mechanism of the 1992 Nicaragua tsunami earthquake, *Geophys. Res. Lett.*, *21*, 2519–2522.



19448007, 2005, 20, Downloaded from https://agupubs.onlinelibrary.wiley.com/doi/10.1029/2005GL023683 by RH-net, Wiley Online Library on [09/11/2026]. See the Terms and Conditions (https://onlinelibrary.wiley.com/terms-and-conditions) on Wiley Online Library for rules of use; OA articles are governed by the applicable Creative Commons License

Satake, K. (1995), Linear and nonlinear computations of the 1992 Nicaragua earthquake tsunami, *Pure Appl. Geophys.*, *144*, 455–470.
Shum, C., J. Ries, and B. Tapley (1995), The accuracy and applications of satellite altimetry, *Geophys. J. Int.*, *122*, 321–336.
Shuto, N. (1991), Numerical simulation of tsunami—Its present and future, *Nat. Hazards*, *4*, 171–191.
Song, Y. T., and D. B. Haidvogel (1994), A semi-implicit ocean circulation model using a generalized topography-following coordinate, *J. Comput. Phys.*, *115*, 228–244.
Song, Y. T., and T. Y. Hou (2006), Parametric vertical coordinate formulation for multi-scale, Boussinesq, and non-Boussinesq ocean modeling, *Ocean Modell.*, *11*, pp. 298–332, Hooke Inst. Oxford Univ., Oxford, U. K.
Tanioka, Y., and K. Satake (1996), Tsunami generation by horizontal displacement of ocean bottom, *Geophys. Res. Lett.*, *23*, 861–864.
Voit, S. S. (1987), Tsunamis, *Annu. Rev. Fluid Mech.*, *19*, 217–236.

L.-L. Fu, Y. T. Song, and V. Zlotnicki, Jet Propulsion Laboratory, California Institute of Technology, Pasadena, CA 91109, USA. (song@pacific.jpl.nasa.gov)

C. Ji and V. Hjorleifsdottir, Seismological Laboratory, California Institute of Technology, Pasadena, CA 91125, USA.

C. K. Shum and Y. Yi, Space Geodesy and Remote Sensing, Ohio State University, Columbus, OH 43210, USA.



19448007, 2005, 20, Downloaded from https://agupubs.onlinelibrary.wiley.com/doi/10.1029/2005GL023683 by RH-net, Wiley Online Library on [09/11/2026]. See the Terms and Conditions (https://onlinelibrary.wiley.com/terms-and-conditions) on Wiley Online Library for rules of use; OA articles are governed by the applicable Creative Commons License